Supporting Information

Surface charge directed borophene - phosphorous nitride nanodot heterojunction support for enhanced photoelectrochemical performance

Experimental Section

### Synthesis of nano-sized phosphorus nitride dots (PNDs)

The PNDs were synthesized by solvo-thermal method. In a typical synthesis, 20 mg phosphonitrilic chloride trimer (PCT) were mixed with 20 mL ethanol and transferred into a teflon lined autoclave and treated at 180 °C for 12 h. After the completion of the hydrothermal reaction, this autoclave was allowed to cool down at room temperature and obtained solution was filtered through 0.22 μm syringe filter, in order to separate the larger particles. The obtained PNDs were kept at room temperature for further use.

Synthesis of 0D Borophene Dots (BDs)

BDs were synthesized by two steps, i.e., sonication and hydrothermal methods. In the first step, a 30 mL of DMF solution containing 30 mg of boron powder was ultrasonicated at 400 W for 5 h to obtain the 2D sheets. Afterwards, the solution was centrifuged for 30 min at 1500 rpm. The brown coloured surfactant containing 2D borophene was decanted to a 50 mL Teflon-lined stainless autoclave for 12h thermal reaction at 180 °C. After the reaction, the suspension was cooled down and filtered through a syringe filter of 0.22 μm to collect the desired size of 0D BDs.

Preparation of PND-BDs hybrid

The PNDs-BDs hybrids were prepared by adding 1 ml of BDs solution to 1 ml of PNDs solution and sonicated for 10 min. The obtained hybrid nanodots were kept at room temperature for further experiments. A detailed schematic of PNDs, BDs and PNDs-BDs hybrid synthesis has been given below in scheme S1.
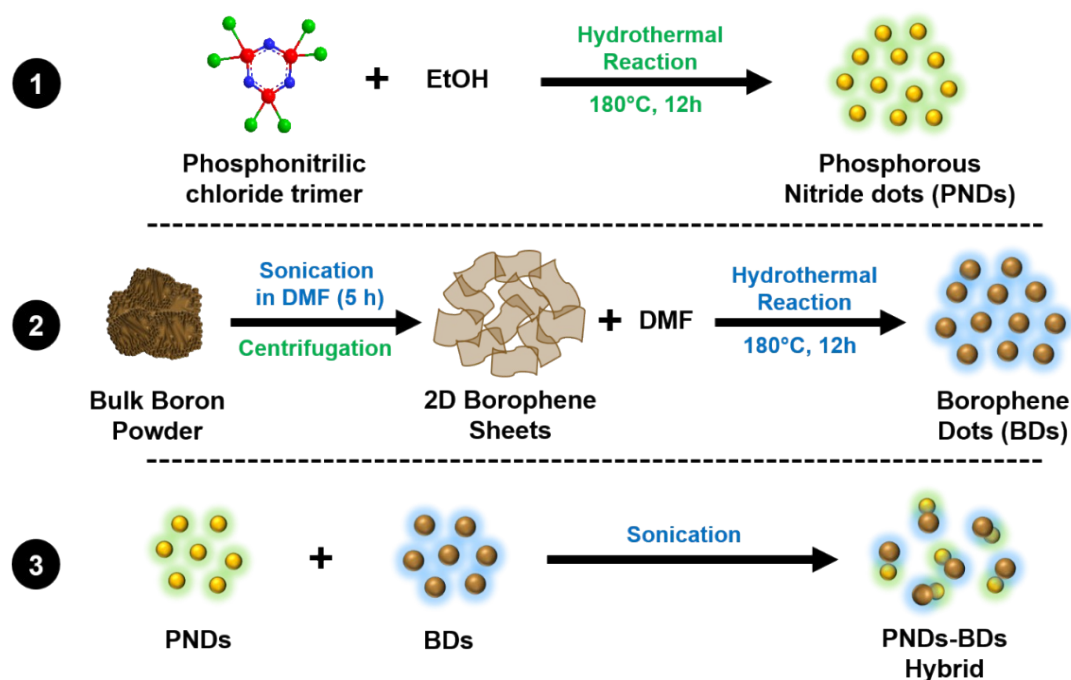
Scheme S1. Step wise synthesis of phosphorous nitride nanodots, borophene nanodots and hybrid nanodots of phosphorous nitride and borophene, respectively.

Synthesis of WO₃ photoanode

Nanoblock featured WO$_3$ photoanode was synthesized directly over fluorine-doped tin oxide (FTO) followed by hydrothermal process. Firstly, two different 15 mL aqueous precursor solutions of sodium tungsten dihydrate (Na$_2$WO$_4$·2H$_2$O) (0.125 g) and ammonium oxalate monohydrate ((NH$_4$)$_2$C$_2$O$_4$·H$_2$O) (0.118 g) were prepared in distilled water. After 30 min of stirring, the colourless tungsten precursor solution was converted to white suspension by drop wise addition of 3M HCl (5 mL), which was again converted to clear solution by adding

ammonium oxalate precursor solution with to it. After half an hour of stirring, the final mixture was decanted to a 50 mL Teflon-lined stainless autoclave for 8h thermal reaction at 140 °C, having well placed FTOs with conducting side faced down. Afterward, the in-situ grown WO_3 samples were cleaned properly with deionized water and dried in oven at 60 °C for 30 min. The WO_3 substrates were annealed at 500 °C in a muffle furnace for 1 hour to obtain WO_3 thin films with monoclinic phase.

Preparation of WO_3/PNDs and WO_3/BDs and WO_3/PNDs-BDs photoanodes

WO_3 photoanodes were prepared according to a reported chemical bath deposition (CBD) method . As prepared WO_3 photoanodes were sensitized in a fixed concentrations of PNDs and BDs solution separately for 10 h at room temperature to fabricate WO_3/PNDs and WO_3/BDs, respectively. After the sensitization process, the films were cleaned with DI water to remove the excess PNDs and BDs at the surface of WO_3 photoanodes. Then the films were then dried at 100°C for 6 h. In order to fabricate WO_3/PNDs-BDs photoanodes, the same CBD process was followed by immersing those WO_3/PNDs photoanodes to BDs solutions for 10h. A detailed schematic of bare WO_3 and composite WO_3/PNDs-BDs photoanodes fabrication has been given below in scheme S2.
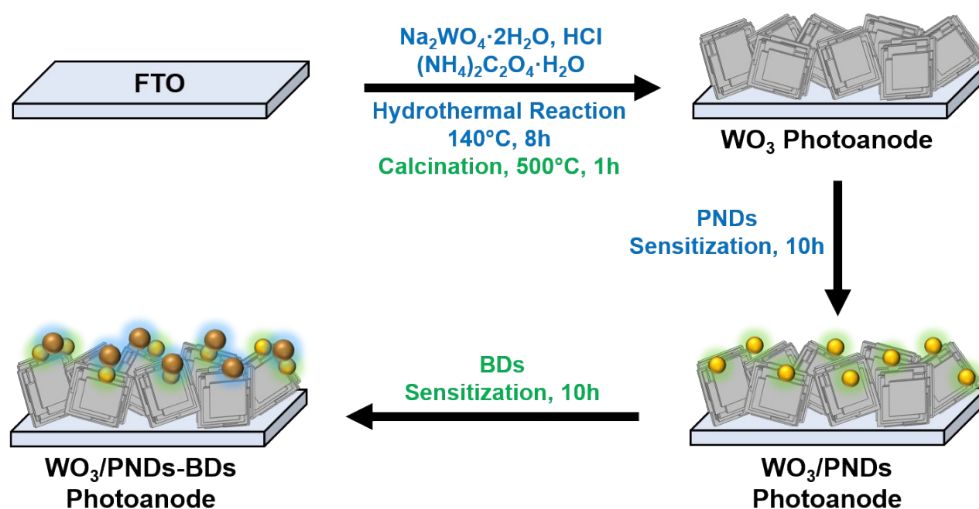
Scheme S2. Step wise fabrication of bare WO_3 and composite WO_3/PNDs-BDs photoanodes.

Fabrication of PNDs photoelectrode

1mL of PNDs (1 mg/mL) solution in ethanol was mixed with 50 μL of Nafion and sonicated for 1 h to make a uniform solution. 50 μL of the above solution was drop-casted over a cleaned FTO substrate and dried at 60 °C for 2 h. This procedure was repeated four times to make the PNDs film. After the drop-casting and drying process, the films were heated at 100 °C for 3 h to obtain the PNDs photoelectrode film.

Fabrication of BDs photoelectrode

1mL of BDs (1 mg/mL) solution in DMF was mixed with 50 μL of Nafion and sonicated for 1 h to make a uniform solution. 50 μL of the above solution was drop-casted over a cleaned FTO substrate and dried at 60 °C for 2 h. This procedure was repeated four times to make the BDs film. After the drop-casting and drying process, the films were heated at 100 °C for 3 h to obtain the BDs photoelectrode film.

Fabrication of PNDs-BDs photoelectrode

Firstly, 50 μL of the above PNDs solution was drop-casted over a cleaned FTO substrate and dried at 60 °C for 2 h. This procedure was repeated two times to make the PNDs film. Secondly, 50 μL of the above BDs solution was drop-casted over the PNDs film and dried at 60 °C for 2 h. This procedure was repeated two times to make the BDs film. After the drop-casting and drying process, the films were heated at 100 °C for 3 h to obtain the PNDs-BDs photoelectrode film.

Material Characterization

The X-ray diffraction (XRD) analysis were carried out by Rigaku SmartLab 9 kW (Cu K_α light source, λ =1.54 Å) having 0.5 °/sec scanning speed. Field emission transmission electron microscopy (FETEM) related analysis were performed through JEOL JEM 2100F microscope with 200 kV operating voltage. The X-ray photoelectron spectroscopy (XPS) analysis were measured through Thermo-Fisher Scientific photoelectron spectrometer (ESCALAB Xi+) equipped with X-ray source (hν = 1486.6 eV) of a monochromatized Al-K_α. The field emission scanning electron microscopy (FESEM) related morphological features of the photoanodes were studied by Zeiss Sigma-300 instrument with 5 kV operating voltage. The UV-Vis absorption spectra were characterized on Shimadzu UV-2600 (Japan) spectrophotometer at room temperature. The photoluminescence (PL) and time-resolved photoluminescence (TRPL) measurements were performed by Horiba Scientific Fluoromax-4 spectrophotometer and Edinburg Lifespec II Instrument, respectively. Zeta potential analysis of nano sized dots were recorded on Malvern Nano-ZS90 ZETASIZER instrument.

Photoelectrochemical Characterizations

Linear sweep voltammetry (LSV), chronoamperometry, electrochemical impedance spectroscopy (EIS) and Mott−Schottky (MS) analysis were performed on GAMRY INTERFACE 1010 E potentiostat using standard three electrode setup having Ag/AgCl electrode as reference and graphite rod as the counter electrode. Na_2SO_4 aqueous electrolyte of 0.1 M (pH=6), purged with N_2 gas was used for PEC measurements. The PEC measurements were analyzed under SCIENCETECH (Class AAA) SciSun-300 solar simulator having 1.5 G Air mass filter. The incident photon to current efficiency (IPCE) analysis was obtained from Newport Oriel IQE-200 instrument. Online gas chromatography (GC) for Faradaic yield of hydrogen and oxygen gas evolution was operated on Nucon 5765 instrument. The measured potentials alteration from Ag/AgCl to reversible hydrogen electrode (RHE) scale can be signified as:

$$E_{RHE} = E_{Ag/AgCl} + 0.059pH + E°_{Ag/AgCl} \quad …………………(1)$$

where E_{RHE}, $E°_{Ag/AgCl}$ are the potentials against RHE and reference Ag/AgCl electrode, respectively.

Results and Discussions

From XRD analysis, the peaks related to cubic phase of PNDs were well defined (figure S1(a)). The boron powder crystallinity is well indexed to JCPDS no 48-0083 and the BDs was confirmed to be amorphous in nature (figure S1(b)). From the XRD analysis of PNDs-BDs hybrid, both crystallinity of PNDs and amorphous nature of BDs are confirmed (figure S1(a)).
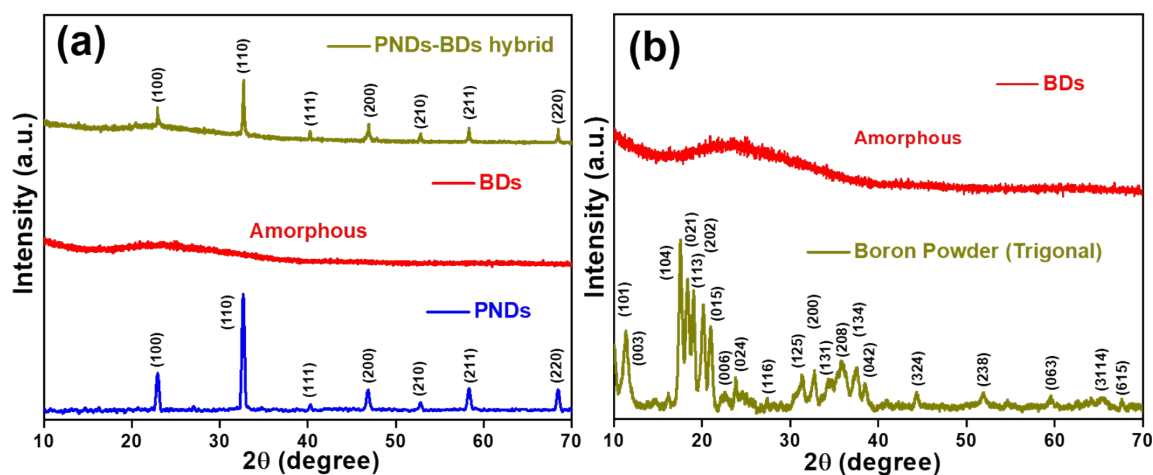

Figure S1. XRD analysis of (a) phosphorous nitride dots (PNDs), borophene dots (BDs) and PNDs-BDs hybrid, (b) crystalline boron powder and amorphous borophene dots (BDs).

Figure S2 is the FETEM image of dispersed PNDs, BDs, PNDs-BDs hybrid nanodots and WO$_3$/PNDs-BDs composite. The well dispersed PNDs with average particle size of 6 nm was confirmed from FETEM analysis (figure S2(a)). The FETEM image of BDs confirms the average particle size of dispersed BDs i.e., 10 nm (figure S2(b)). The prepared hybrid nanodots of PNDs and BDs were confirmed by the FETEM (figure S2(c)). Figure S2(d) is the FETEM image of the WO$_3$/PNDs-BDs composite photoanode.
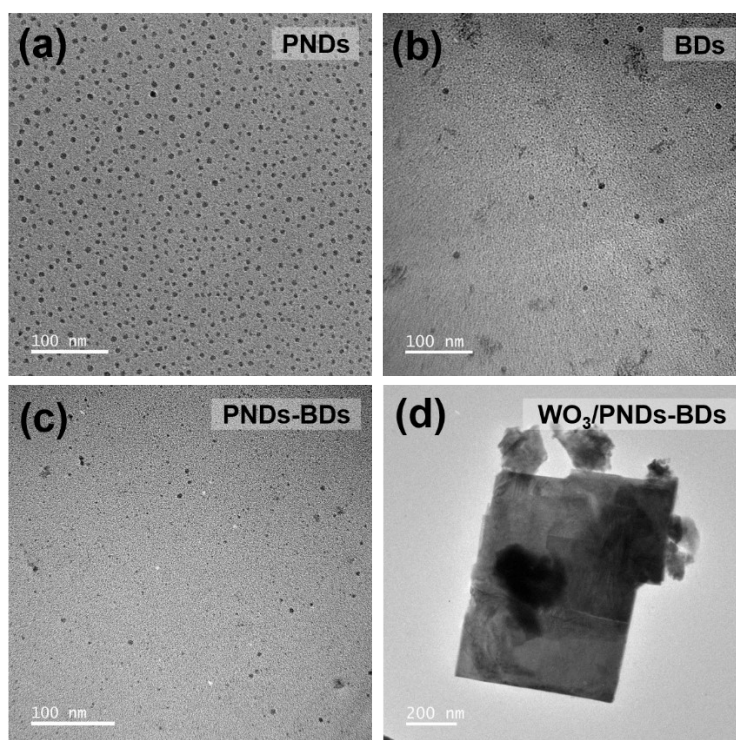

Figure S2. FETEM image of (a) PNDs, (b) BDs, (c) PNDs-BDs hybrid and (d) WO$_3$/PNDs-BDs composite.

The decay patterns in TRPL have been fitted with bi-exponential function and the average lifetime of these nanodots can be calculated as follows:

$$< \tau > \ = \ \frac{a_1\tau_1^2 + a_2\tau_2^2}{a_1\tau_1 + a_2\tau_2}$$ …………………………..(2)

Table S1. TRPL fitted parameters of PNDs, BDs and PNDs-BDs hybrid.

Materials	τ_1	τ_2	α_1	α_2	$\langle\alpha\rangle$ (ns)
PNDs	1.798	4.419	32.224	67.776	3.99
BDs	1.915	9.137	32.369	67.631	8.48
PNDs-BDs hybrid	1.963	6.669	42.361	57.639	5.83

The XPS valence band spectra of PNDs and BDs was analyzed to gain insight the proper band positions, as shown in figure S3. The valence bands (VB) for PNDs and BDs were noted to be at 2.8 eV and 2.5 eV.
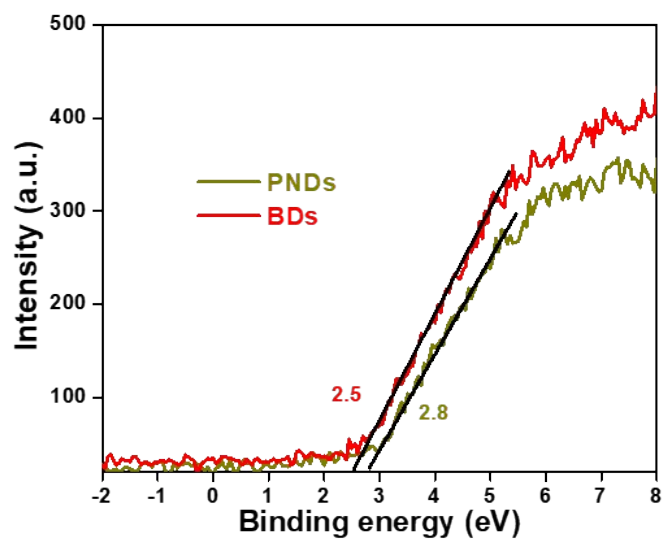

Figure S3. XPS valence band spectra of PNDs and BDs.

The absorption peaks for PNDs and BDs were recorded to be at 348 nm and 354 nm, respectively (figure S4(a)). These absorption peaks are related to 3.06 eV and 3.26 eV bandgaps for PNDs and BDs, respectively (figure S4(b)).
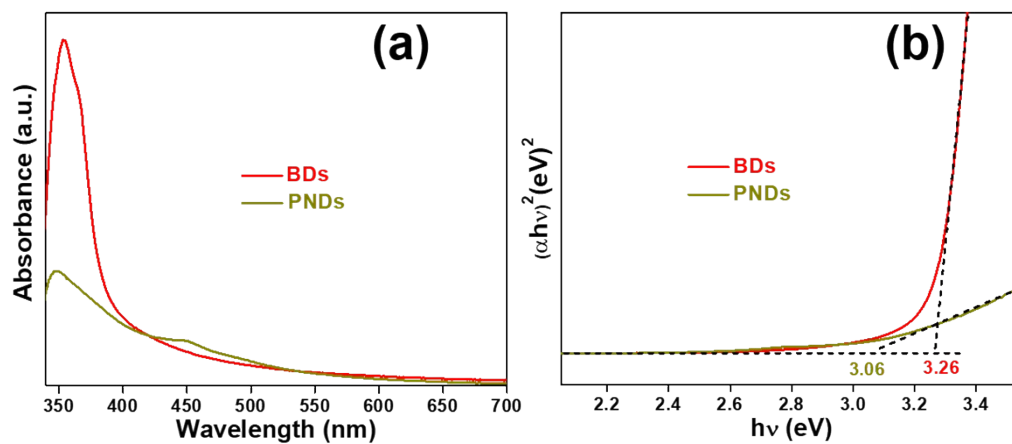

Figure S4. (a) UV-visible absorption spectra and the corresponding (b) Tauc's plots of PNDs and BDs.

All the peaks of bare WO$_3$ photoanode are well matched with peaks of JCPDS no. 00-005-0364, which confirms the monoclinic phase of WO$_3$ (figure S5).
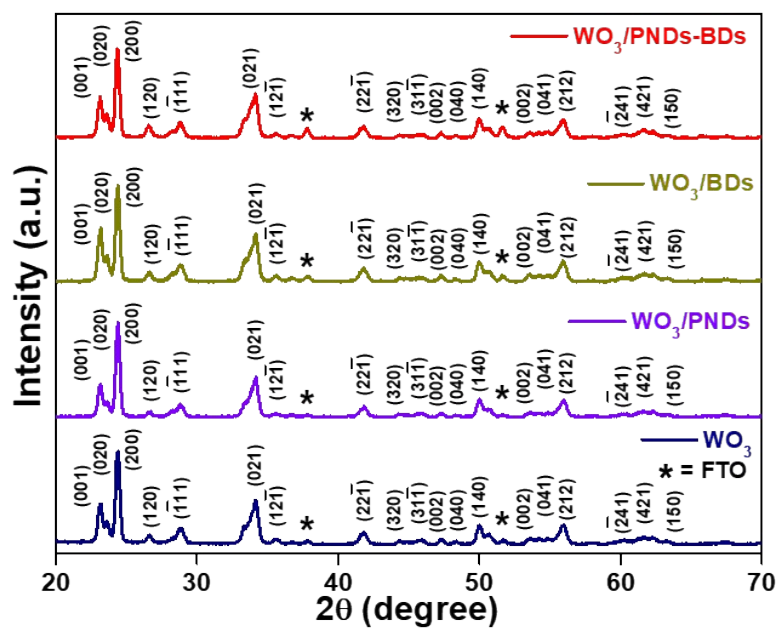

Figure S5. XRD analysis of WO$_3$, WO$_3$/PNDs, WO$_3$/BDs and WO$_3$/PNDs-BDs photoanodes.

FESEM image of bare WO_3 thin film evidences the uniformly grown nanoblock shaped WO_3 with average size of 800 nm above the FTO (figure S6(a)). Morphology of WO_3 photoanode was not altered with PNDs and BDs modifications, as shown in figures S6(b), figure S6(c). Figure S6(d) is the cross-sectional view of WO_3/PNDs-BDs composite, which attributes the vertically grown WO_3 blocks above the FTO surface.
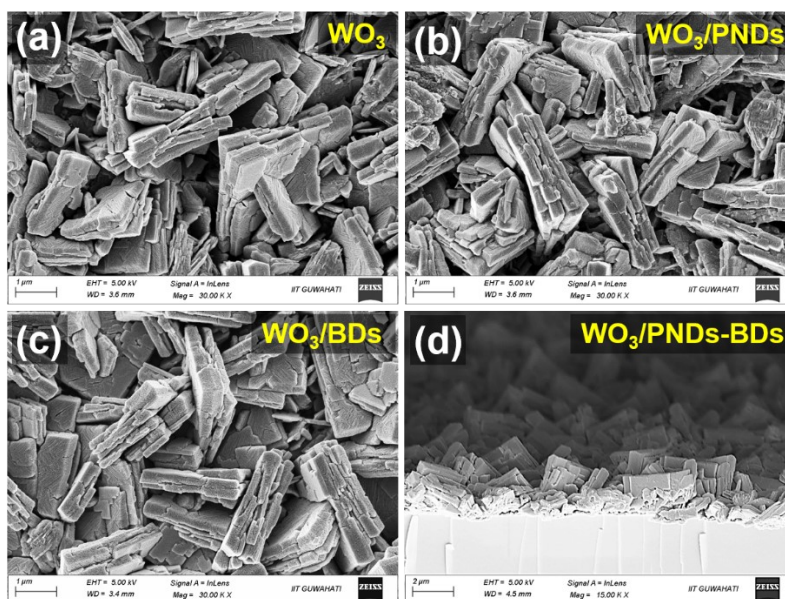

Figure S6. FESEM image of (a) WO_3, (b) WO_3/PNDs, (c) WO_3/BDs; and (d) Cross-sectional FESEM image of WO_3/PNDs-BDs photoanode.

Uniformly distributed individual W, O, P, N and O elements were confirmed from the elemental mapping by scanning transmission electron microscopy (STEM) (figure S7(i)- figure S7(vi)).
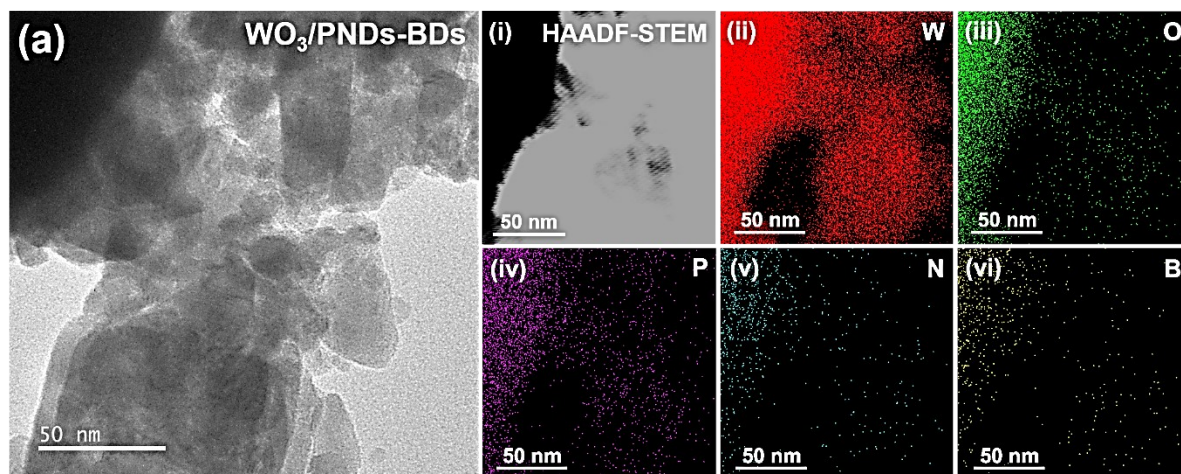

Figure S7. (a) FETEM image of WO$_3$/PNDs-BDs composite; (i) STEM image and corresponding individual EDS mapping figures of WO$_3$/PNDs-BDs having (ii) W, (iii) O, (iv) P, (v) N , (vi) B.

To study the surface area and pore volume, we have analyzed the N_2 adsorption/desorption isotherms and pore size distribution curves for bare WO_3 and modified WO_3/PNDs-BDs composite (figure S8). The surface area and the pore volume of WO_3/PNDs-BDs structures were 2.3 times and 3 times higher than the bare WO_3 structure, respectively. All the parameters have been provided below in table S2.
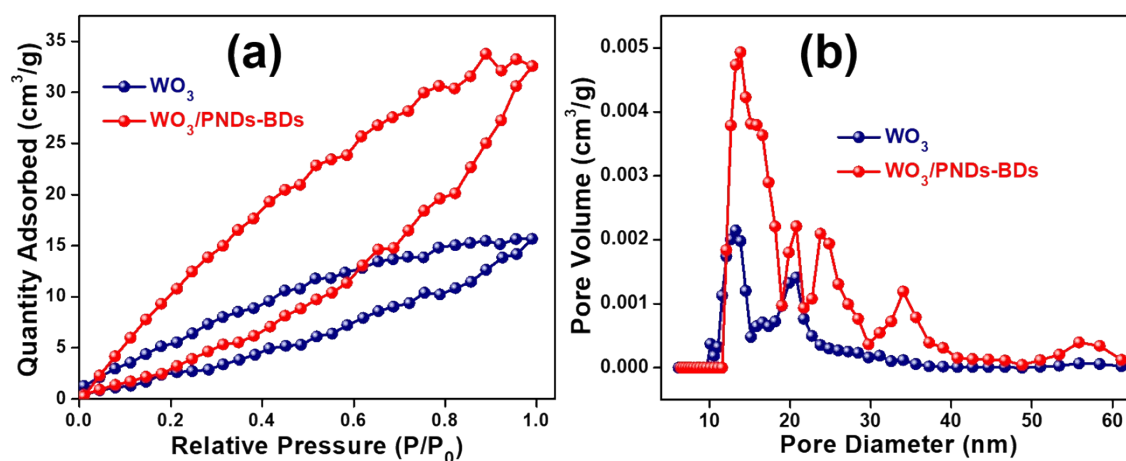

Figure S8. (a) N_2 adsorption/desorption isotherms and (b) pore size distribution curves for bare WO_3 and modified WO_3/PNDs-BDs composite.

Table S2. Surface area and pore volume parameters of WO_3 and WO_3/PNDs-BDs.

Photoanodes	Surface Area (m^2/g)	Pore Volume (cm^3/g)
WO_3	13.1	0.005
WO_3/PNDs-BDs	29.5	0.015

The peaks at 35.77 eV for $4f_{7/2}$ and 37.79 eV for $4f_{5/2}$ attributes to the +6 oxidation state of W in WO_3 photoanode (figure S9(b)). The O 1s spectra of WO_3 is having two signals at 530.17 eV related to lattice oxygen (O_L) and 531.35 eV related to oxygen vacancies (O_V) (figure S9(c)). Figure S9(a) represents the XPS survey spectra of composite photoanode having the corresponding characteristic signals of W, O, P, N and B. A small shift in positions of $4f_{7/2}$, $4f_{5/2}$, and O_L towards lower binding energies indicates the electronic interactions within the base semiconductor and the nanodots. Also, the shift in signals of other elements P, N and B for WO_3/PNDs-BDs photoanode compared to PNDs, BDs and PNDs-BDs hybrid proves the electronic interactions among those components of the composite (figure S9(d), figure S9(e), figure S9(f)).
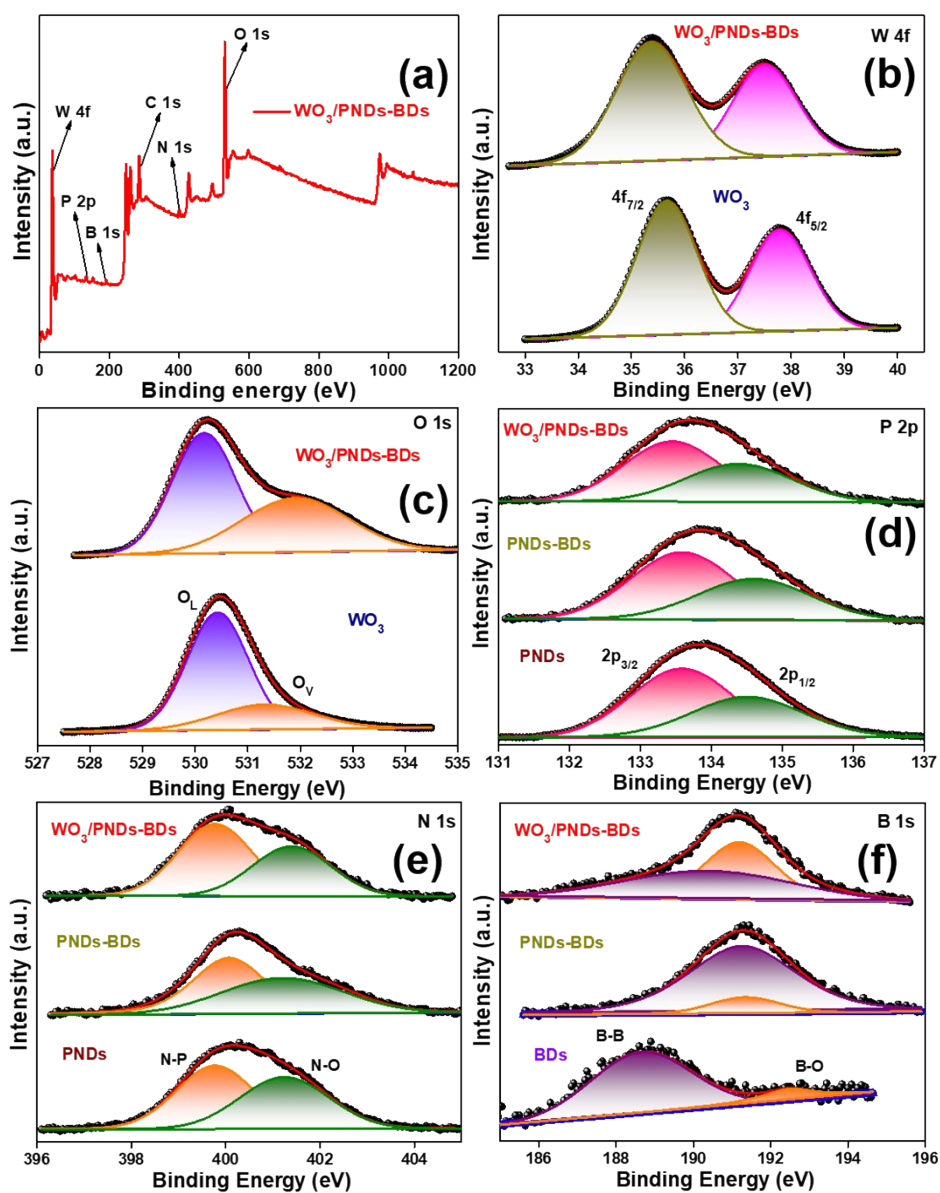
Figure S9. (a) XPS survey spectra of fabricated WO₃/PNDs-BDs photoanode; Core level XPS spectra of (b) W 4f, (c) O 1s (d) P 2p, (e) N 1s and (f) B 1s.

The absorption edges and bandgaps for bare and other modified photoanodes were noted to be at ~ 393 nm and ~ 2.82 eV, respectively, which indicates that the modification with PNDs and BDs doesn't have any impact on the optical properties of WO_3 photoanode (figure S10).
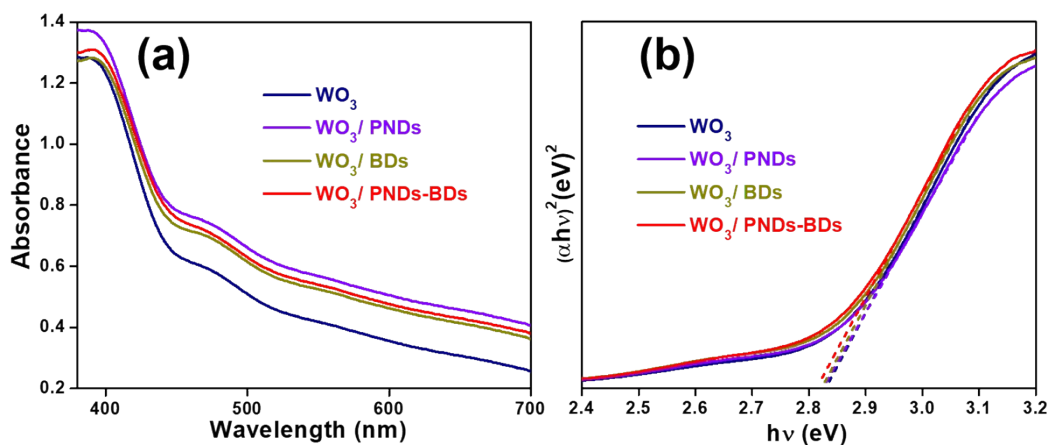

Figure S10. (a) UV-visible absorption spectra and the corresponding (b) Tauc's plots of WO_3, WO_3/PNDs, WO_3/BDs and WO_3/PNDs-BDs photoanodes.
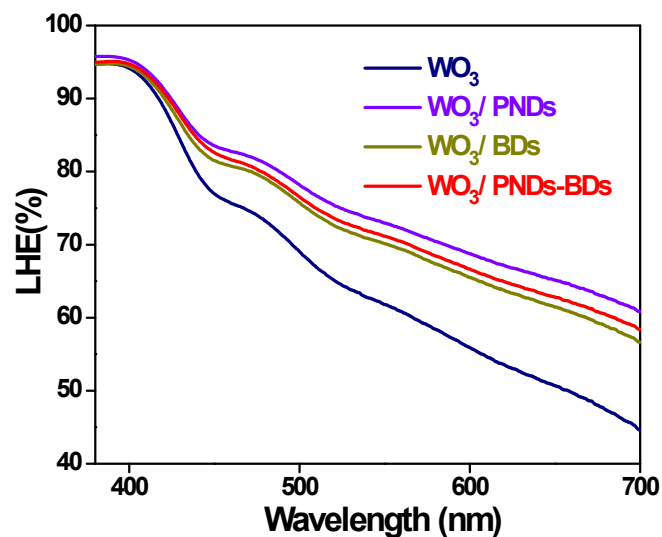
Figure S11. Light-harvesting efficiency (LHE) spectra of WO$_3$, WO$_3$/PNDs, WO$_3$/BDs and WO$_3$/PNDs-BDs photoanodes.

Table S3. TRPL fitted parameters of WO$_3$ and WO$_3$/PNDs-BDs photoanodes.

Photoanode	τ_1	τ_2	α_1	α_2	$\langle\alpha\rangle$ (ns)
WO$_3$	1.429	6.673	91.506	8.494	11.61
WO$_3$/PNDs-BDs	0.805	2.113	71.384	28.616	5.32

The dual nanodots sensitized (i.e., PNDs and BDs) WO_3 photoanode gives a maximum current density of 2.8 mA/cm^2 @ 1.23 V vs RHE. The optimization of BDs loading over WO_3/PNDs photoanodes has been provided in figure S12. A high 4 fold increment in current density of pristine WO_3 photoanode due to PNDs and BDs sensitizations approves the maximized charge separation and minimized charge recombination towards high PEC water oxidation performance.
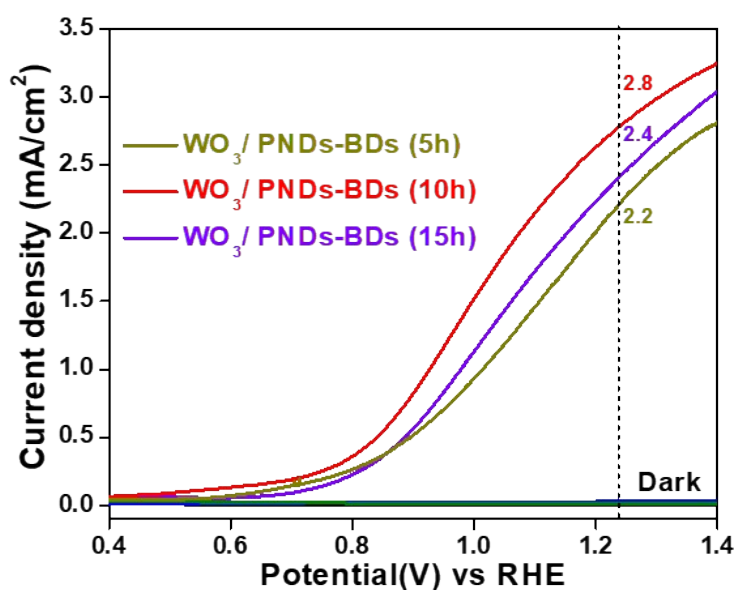

Figure S12. LSV curves WO_3/PNDs-BDs photoanodes with respect to different dipping time for loading BDs over WO_3/PNDs. All these LSV measurements were operated in 0.1M Na_2SO_4 electrolyte under 1 Sun illumination @ 1.23 V vs. RHE.

To know the photo response behaviour of WO_3 photoanode, chronoamperometry analysis of WO_3, WO_3/PNDs, WO_3/BDs and WO_3/PNDs-BDs photoanodes were carried out under 1 Sun light ON and OFF state at 1.23 V vs RHE (figure S13). The anodic spikes of WO_3 photoanode were diminished significantly due to the incorporation of PNDs and BDs which indicates the minimization of photogenerated carrier recombination due to type II heterojunction approach.
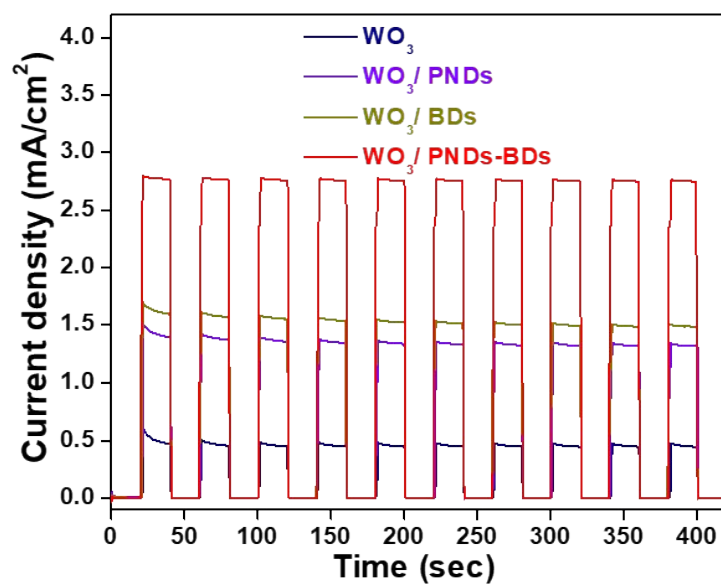

Figure S13. Chronoamperometry curves of WO_3, WO_3/PNDs, WO_3/BDs and WO_3/PNDs-BDs photoanodes under 1 Sun illumination in 0.1 M Na_2SO_4 electrolyte at 1.23 V vs RHE.

The chronoamperometry analysis of PNDs, BDs and PNDs-BDs thin-films were carried out to know the photo-response property (figure S14). Although PNDs and BDs show a very less current densities in $\mu A/cm^2$ as compared to current density of WO_3 thin-film, still the light harvesting capability of photo responsive material PNDs and BDs is confirmed. As the photo-response property of PNDs-BDs hybrid is higher (~ 0.2 $\mu A/cm^2$) as compared to the individual photo-response property of PNDs (~ 0.1 $\mu A/cm^2$) and BDs (~ 0.1 $\mu A/cm^2$), that indicates the maximized charge separation and minimized charge recombination due to formation PNDs-BDs hybrid.
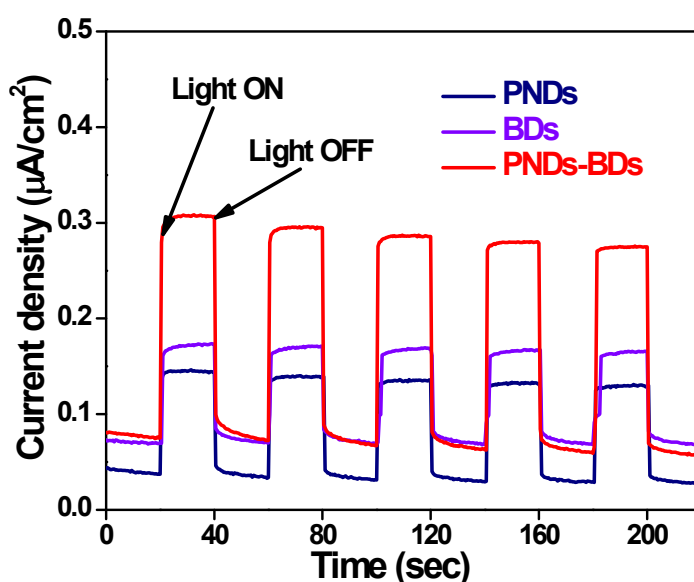

Figure S14. Chronoamperometry curves of PNDs, BDs and PNDs-BDs under 1 Sun illumination in 0.1 M Na_2SO_4 electrolyte at 1.23 V vs RHE.

Table S4. Fitting parameters for Nyquist plots and total charge carrier densities of WO_3, WO_3/PNDs, WO_3/BDs and WO_3/PNDs-BDs photoanodes.

Photoanode	$R_s(\Omega)$	$R_{trap}(\Omega)$	$C_{bulk}(\mu F)$	$R_{ct}(\Omega)$	$C_{trap}(\mu F)$	$N_D(cm^{-3})$
WO_3	51.8	80.9	26.0	1906	14.9	**1.5×10^{20}**
WO_3/PNDs	46.6	77.4	27.9	1374	15.5	2.1×10^{20}
WO_3/BDs	43.4	75.7	30.6	1293	16.4	2.5×10^{20}
WO_3/ PNDs-BDs	38.4	72.4	31.6	978	18.1	**4.0×10^{20}**

Figure S15 shows the Nyquist plots for PNDs, BDs and PNDs-BDs films having experimental data and fitted data w.r.t. equivalent circuit model (inset in figure S15). The radius of semicircles related to PNDs and BDs films are smaller due to the formation of PNDs-BDs hybrid. The equivalent circuit model comprises series resistance (R_s), bulk charge trapping resistance (R_{trap}) and semiconductor/electrolyte charge transfer resistance (R_{ct}). The equivalent circuit parameters related to Nyquist plots for the photoanodes are provided below in table S5. The R_{ct} value for PNDs and BDs were reduced from 241 kΩ and 163 kΩ to 15 kΩ due to PNDs-BDs formation. These results confirm the improved charge transfer properties are due to formation of type II heterojunction based PNDs-BDs hybrid.
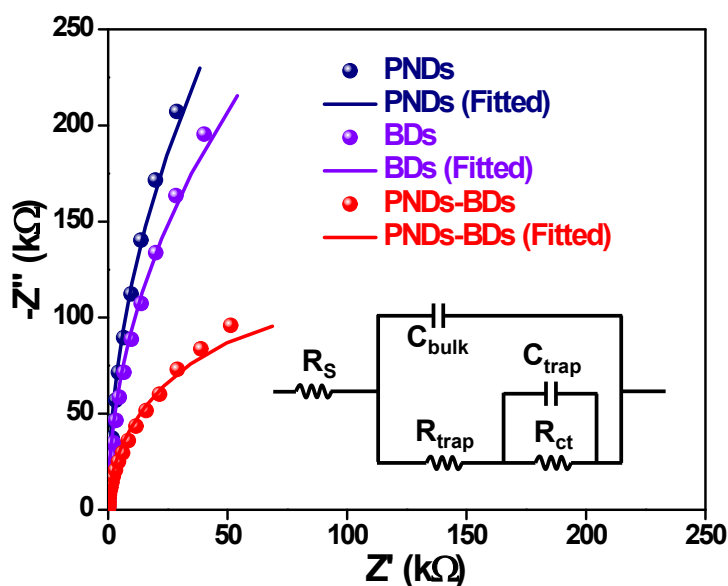

Figure S15. Nyquist plots of PNDs, BDs and PNDs-BDs electrodes having their fitted curves w.r.t. equivalent circuit model under 1 Sun illumination at 1.23 V vs RHE.

Table S5. Fitting parameters for Nyquist plots of PNDs, BDs and PNDs-BDs thin films.

Electrodes	$R_s(\Omega)$	$R_{trap}(k\Omega)$	$R_{ct}(k\Omega)$
PNDs	33.9	1173	241
BDs	40.7	751	163
PNDs-BDs	34.8	187	15

The MS-analysis was carried out to know the change in total carrier density (N_D) of WO$_3$ photoanode with PNDs and BDs modifications, as shown in figure S16. The positive slops confirm the n-type conductivity of the bare and modified photoanodes. The charge carrier density can be calculated as follows:

$$\frac{1}{C^2} = \frac{1}{A^2 N_D e \varepsilon \varepsilon_0}[E - E_{FB} - \frac{kT}{e}]$$ ....(3)

The exposed surface area, flat-band potential, dielectric constant and capacitance of the photoanode are A, E$_{FB}$, ε and C, respectively. The permittivity of vacuum is ε$_0$, the applied bias is E, the Boltzmann constant is k, the temperature is T and the charge of electron is e. The calculated charge carrier densities are 1.5 $\times$ 10^{20} cm^{-3} for WO$_3$ photoanode, 2.1 $\times$ 10^{20} cm^{-3} for WO$_3$/PNDs photoanode, 2.5 $\times$ 10^{20} cm^{-3} for WO$_3$/BDs photoanode and 4 $\times$ 10^{20} cm^{-3} for WO$_3$/PNDs-BDs photoanode, respectively. The synergistic effects between positively charged PNDs and negatively charged BDs provides improved charge carrier densities to WO$_3$ photoanode, which facilitate the electrical conductivity of the photoanode for higher oxidation activity.
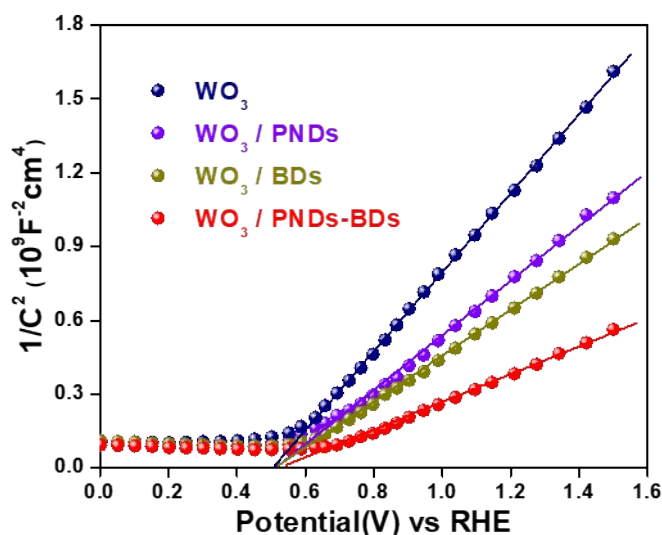

Figure S16. Mott−Schottky plots of WO$_3$, WO$_3$/PNDs, WO$_3$/BDs and WO$_3$/PNDs-BDs photoanodes.

From the Mott-Schottky analysis, the Fermi levels for WO_3, PNDs and BDs were found to be at 0.5 eV, 0.1 eV and -0.1 eV, respectively (figure S16 and figure S17).
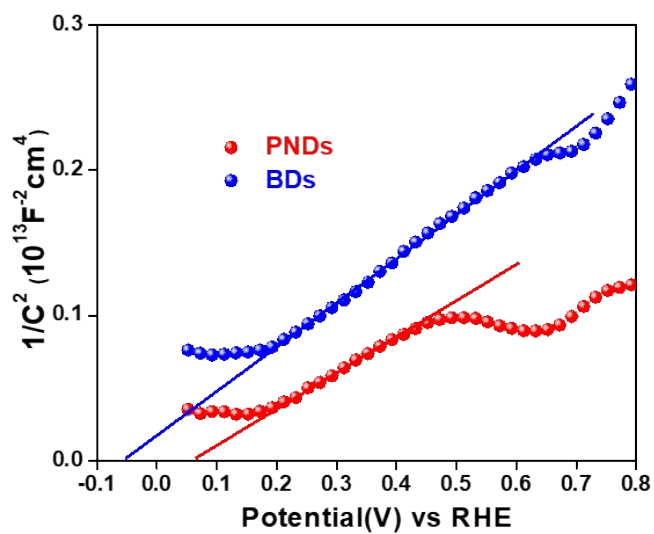

Figure S17. Mott−Schottky plots of PNDs and BDs.

To know the improvement in charge separation efficiency (η_{sep}) and charge injection efficiency (η_{inj}) by PNDs and BDs modifications on WO_3 photoanode, hole scavenger (HS) test of the photoanodes was performed under 1 Sun illumination in 0.1 M Na_2SO_4 electrolyte having 0.03 M Na_2SO_3 hole scavenger (figure S18). The current densities from LSV data were recorded to be ~ 2.9, ~ 1.5, ~ 1.4 and ~ 1.1 times higher in presence of hole scavenger in comparison to corresponding photoanodes in absence of the hole scavenger for WO_3, WO_3/PNDs, WO_3/BDs and WO_3/PNDs-BDs photoanodes, respectively (figure S18(a) and figure S18(b)). A very high enhancement in current density for WO_3 photoanode in comparison to other modified photoanodes confirms the maximized electrical conductivity due to modification with PNDs and BDs over WO_3 film. The photocurrent density arising from water splitting (J_{H_2O}), η_{sep}, and η_{inj} can be described as follows:

$$J_{H_2O} = J_{abs} * \eta_{sep} * \eta_{inj} \quad \ldots\ldots\ldots\ldots\ldots\ldots (4)$$

$$\eta_{sep} = \frac{J_{Na_2SO_3}}{J_{abs}} \quad \ldots\ldots\ldots\ldots\ldots\ldots\ldots..(5)$$

and

$$\eta_{inj} = \frac{J_{H_2O}}{J_{Na_2SO_3}} \quad \ldots\ldots\ldots\ldots\ldots\ldots.(6)$$

where J_{abs} is the photocurrent density of photoanode at complete conversion of absorbed photon to current. J_{H_2O} and $J_{Na_2SO_3}$ are the photocurrent densities obtained in 0.1 M Na_2SO_4 electrolyte without and with 0.03 M Na_2SO_3 hole scavenger, respectively.

The calculated η_{sep} of WO_3 was enhanced from 51 % to 56 % for WO_3/PNDs, 60 % for WO_3/BDs and 77 % for WO_3/PNDs-BDs photoanodes (figure S18(c)), which attributes the

better and faster charge separation ability of WO_3 due to dual incorporations of PNDs and BDs.

Similarly, an enhanced η_{inj} of WO_3 from 35 % to 67 % for WO_3/PNDs, 72 % for WO_3/BDs and maximum 91 % for WO_3/PNDs-BDs photoanodes (figure S18(d)), results a maximized charge transport property at photoanode/electrolyte interface and minimized photogenerated carriers recombination of WO_3 photoanode due to the dual nanodots modifications. The very low 35 % of η_{inj} with high 51 % of η_{sep} indicates the sluggish PEC activity of WO_3 photoanode, whereas the significant improvement in η_{inj} up to 91 % with PNDs and BDs incorporations attributes the surface charge induced heterojunction approach for boosted PEC water oxidation performance.
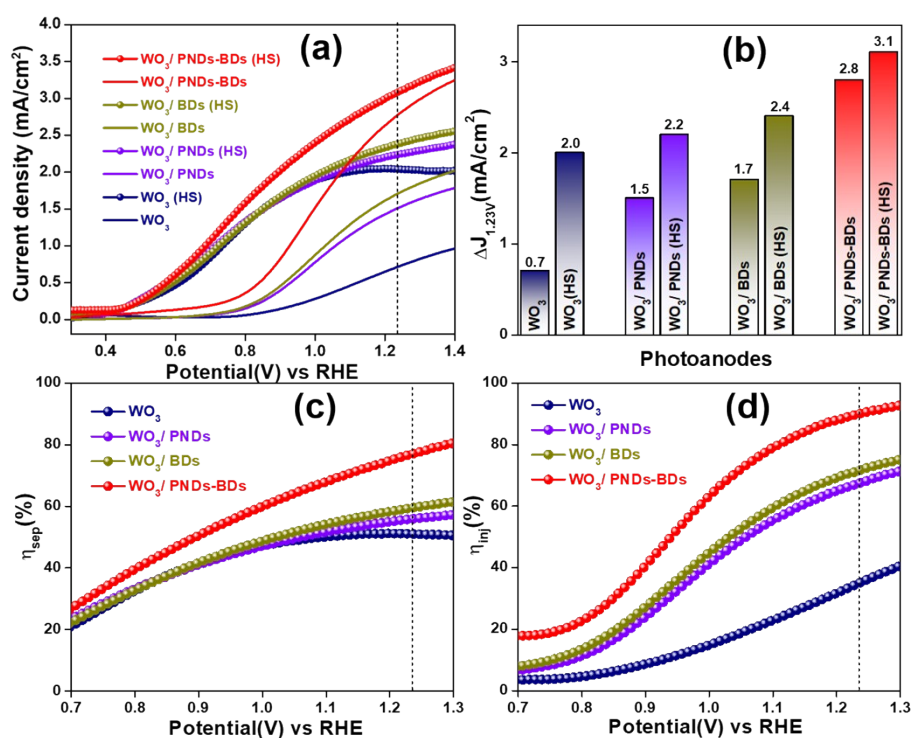

Figure S18. (a) LSV curves in presence of hole scavenger (Na_2SO_3) in Na_2SO_4 electrolyte; (b) Current density based bar diagram at 1.23 V vs RHE of the photoanodes with and without hole scavenger; charge (c) separation and (d) injection efficiencies of the photoanodes under 1 Sun illumination.

APCE and IPCE for the photoanodes was analyzed to evaluate the change in current conversion efficiency of WO_3 photoanodes with dual incorporations of PNDs and BDs over the surface, as shown in figure S19. The IPCE of WO_3 thin film was maximized from 16 % to 31 %, 36 % and a maximum 56 % with PNDs, BDs and PNDs-BDs modifications, respectively, which confirms the better photocatalytic property of WO_3/PNDs-BDs photoanode in comparison to other unmodified and single modified WO_3 photoanodes. The IPCE details evidence the improved PEC water oxidation performance of WO_3 photoanode offered by the synergistic effects between positively charged PNDs and negatively charged BDs.
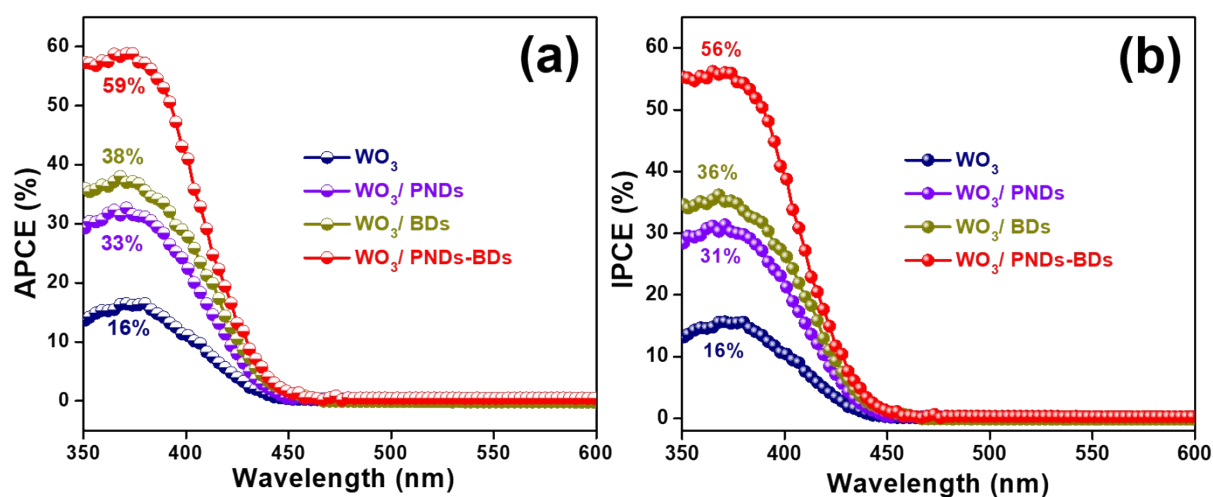

Figure S19. (a) APCE and (b) IPCE plots of WO_3, WO_3/PNDs, WO_3/BDs and WO_3/PNDs-BDs photoanodes.

To examine the operational stability, the chronoamperometry analysis of the photoanodes was performed for 10h (figure S20). After 10h of analysis, the WO_3, WO_3/PNDs, WO_3/BDs and WO_3/PNDs-BDs photoanodes were stabilized up to a very less 20 %, average of 75 % and 80 % and a very high 90 %, respectively, w.r.t. initial corresponding photocurrent densities. The modifications with PNDs and BDs, provides a significant enhanced photostability to WO_3 photoanode.
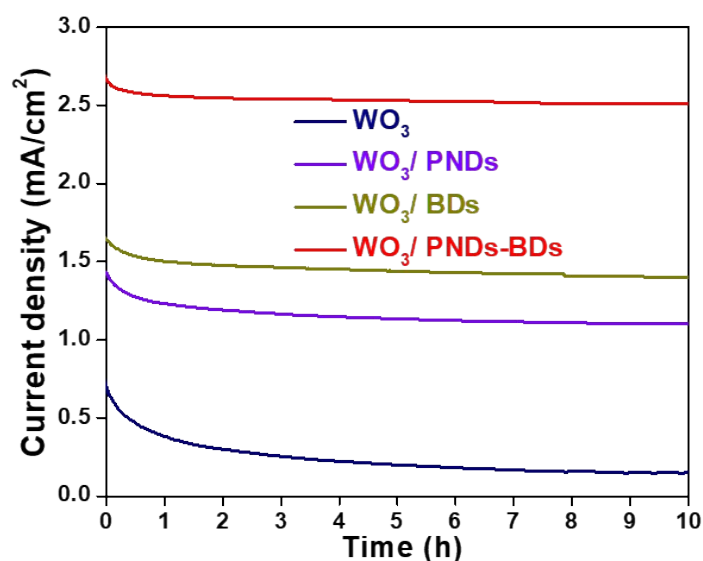

Figure S20. Photo-stabilities of 10h for WO_3, WO_3/PNDs, WO_3/BDs and WO_3/PNDs-BDs photoanodes under 1 Sun illumination at 1.23 V vs RHE.

From the XPS valence band spectra analysis, the valence band of WO_3 photoanode was calculated to be at 2.9 eV (figure S21).
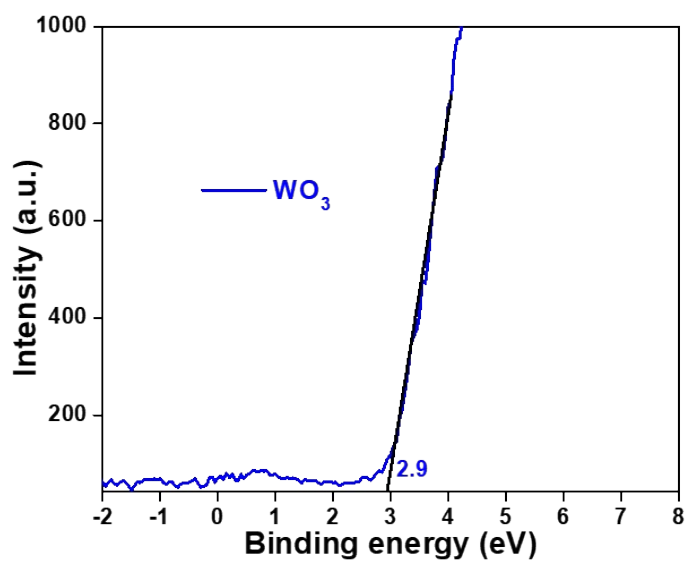

Figure S21. XPS valence band spectra of WO_3.

The schematic of the composite photoanode formation, followed by type-II-II′ heterojunctions, has been shown in figure S22.
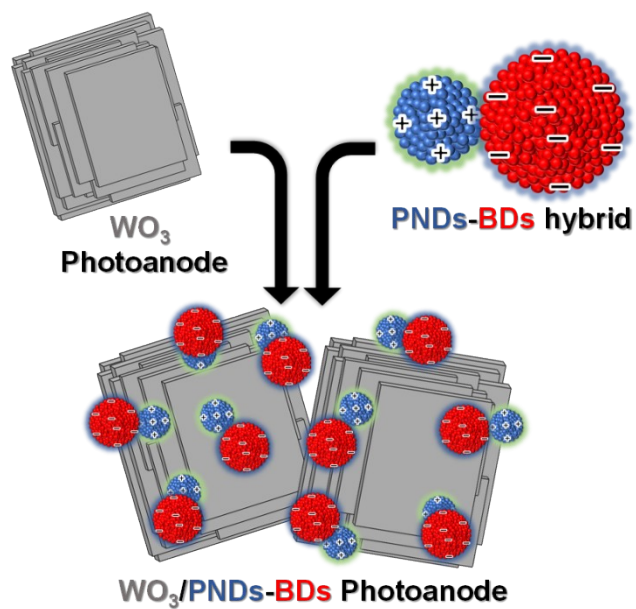

Figure S22. Schematic for the formation of the WO$_3$/PNDs-BDs hybrid.

Table S6. Recent progress on PEC performance of various WO_3 based photoanodes.

Photoanode	Current density (@ 1.23 V vs RHE)	Synthesis method	Reference
$WO_3/BiVO_4$	2.3 mA/cm^2	Hydrothermal	J. Mater. Chem. A, 2018, **6**, 2585–2592
$NiFe/CQD/WO_3$	1.43 mA/cm^2	Hydrothermal	ChemSusChem 2019, **12**,4685−4692
$Mo-WO_3/Fe-WO_3/Bi_2S_3$	2.55 mA cm^2	Hydrothermal	J. Mater. Chem. A, 2020, **8**, 6256–6267
$WO_3/BNQDs$	1.63 mA/cm^2	Hydrothermal	ACS Appl. Energy Mater. 2019, **2**, 7457−7466
$WO_3@CoWO_4$	0.76 mA/cm^2	Hydrothermal	J. Mater. Chem. A, 2018, **6**, 6265–6272
$WO_3/PNDs$	0.81 mA/cm^2	Hydrothermal	Chem. Commun., 2021, **57**, 6157–6160
$WO_3/Ba_2Bi_{1.4}Nb_{0.6}O_6$	2.23 mA/cm^2	Hydrothermal	Adv. Energy Mater., 2018, **8**, 1701655
$WO_3/PNDs-BDs$	**2.8 mA/cm^2 at 1.23 V$_{RHE}$**	**Hydrothermal**	**Present Work**

References

S1. B. Jin, E. Jung, M. Ma, S. Kim, K. Zhang, J. I. Kim, Y. Son and J. H. Park, *J. Mater. Chem. A*, 2018, **6**, 2585–2592.

S2. X. Cao, C. Xu, J. Ma, Y. Dong, C. Dong, M. Yue and Y. Ding, *ChemSusChem*, 2019, **12**, 4685–4692.

S3. Y. Li, Z. Liu, J. Li, M. Ruan and Z. Guo, *J. Mater. Chem. A*, 2020, **8**, 6256–6267.

S4. M. K. Mohanta, T. K. Sahu, D. Gogoi, N. R. Peela and M. Qureshi, *ACS Appl. Energy Mater.*, 2019, **2**, 7457–7466.

S5. H. Y. Zhang, W. J. Tian, Y. G. Li, H. Q. Sun, M. O. Tadé and S. B. Wang, *J. Mater. Chem. A*, 2018, **6**, 6265–6272.

S6. T. K. Sahu, S. Alam, S. Bhowmick, M. K. Mohanta, M. Qureshi, *Chem. Commun.*, 2016, **8**, 563– 568.

S7. B. Weng, C. R. Grice, J. Ge, T. Poudel, X. Deng and Y. Yan, *Adv. Energy Mater.*, 2018, **8**, 1701655.